THE ASTROPHYSICAL JOURNAL, 415:875–881, 1993 October 1

IN-FLIGHT PERFORMANCE AND PRELIMINARY RESULTS FROM THE FAR ULTRAVIOLET SPACE TELESCOPE (FAUST) FLOWN ON ATLAS-1

STUART BOWYER,[1] TIMOTHY P. SASSEEN, MICHAEL LAMPTON,[2] AND XIAOYI WU
Center for EUV Astrophysics, 2150 Kittredge Street, University of California, Berkeley, CA 94720
Received 1993 January 29; accepted 1993 April 6

ABSTRACT

In 1992 March the Far Ultraviolet Space Telescope was flown as part of the NASA ATLAS-1 mission. We describe the in-flight instrument performance and provide a preliminary view of some of the results. Twenty-two wide-field far-ultraviolet images were obtained. At this stage of our analysis, we have far-ultraviolet photometry for more than 4800 sources; the overwhelming majority of these are below the *TD-1* satellite far-ultraviolet detection limit. In these images, we detect sources to a flux limit of 1×10^{-14} ergs s^{-1} cm^{-2} $Å^{-1}$, which is at least an order of magnitude more sensitive than the *TD-1* satellite, and we have virtually complete source detections to a level of 6×10^{-14} ergs s^{-1} cm^{-2} $Å^{-1}$. Among the sources detected, we have identified a subset which show substantial far-ultraviolet excess.

Subject headings: artificial satellites, space probes — instrumentation: detectors — telescopes — ultraviolet: general — ultraviolet: stars

1. INTRODUCTION

The far-ultraviolet band from 1200 to 2000 Å has been increasingly well-studied by a variety of space instruments, including *IUE*, the *TD-1* satellite, the space shuttle ASTRO mission, and the *Hubble Space Telescope*. The Far Ultraviolet Space Telescope (FAUST) is a wide field-of-view telescope that complements these other ultraviolet instruments. The FAUST instrument was flown on-broad the space shuttle *Atlantis* in 1992 March as part of NASA's ATLAS-1 shuttle mission (Craven & Torr 1988).

FAUST is a wide-field (7°.6 diameter) telescope designed to image diffuse and point sources in the wavelength range 1400–1800 Å. The FAUST optical design is an all-reflecting Wynne camera (Wynne 1969). FAUST's optical performance and mechanical construction have been described in Deharveng et al. (1979). The instrument is shown diagrammatically in Figure 1.

The original version of the instrument, which employed an image-intensified film camera, flew on-board Spacelab I (Bixler et al. 1984). On this flight, no useful data were obtained, because of sporadically high geophysical backgrounds. At that time, the instrument lacked the time resolution to allow it to exclude data segments containing geophysical contamination. A major upgrade of the system was achieved with the addition of a photon-counting microchannel plate detector with a wedge-and-strip position-sensitive encoding scheme (Lampton et al. 1986; Siegmund et al. 1987). The wavelength coverage was chosen to block strong atmospheric emission lines shortward of 1400 Å, in particular the H I Lyman-α at 1216 Å and O I lines at 1304 and 1356 Å. This was accomplished by employing multilayer coatings on the instrument's calcium fluoride entrance window. The long-wavelength cutoff was provided by the cesium iodide photocathode film vacuum deposited onto the detector's microchannel plate. The theoretical performance of the improved instrument is described in Lampton, Deharveng, & Bowyer (1990).

We report here the performance of the instrument in flight, the data reduction process, and an overview of some of the first results. During the mission, we observed 22 astronomical targets, described here; three nights of downlooking earth airglow measurements are reported elsewhere (Chakrabarti et al. 1993).

2. CALIBRATION

A preflight calibration was performed in the laboratory. The instrument sensitivity was placed on the absolute scale by comparing the flux measured in a beam by a flux standard reference photodiode detector with that measured by the instrument after the beam had passed through FAUST's optical system. This measurement was performed at 11 wavelengths in the far-ultraviolet. The results are shown in Figure 2. The points are connected by straight lines, and the error bars indicate laboratory measurement uncertainties. We determined the overall grasp of the instrument in flight through comparison of the laboratory calibration of FAUST's measurement of stellar fluxes with *IUE* measurements, as discussed below. We have scaled the data in Figure 2 by a single factor of 0.6 to make the grasp agree with the inflight calibration. No postflight calibration is available because the detector was damaged during the mission.

3. DATA ACQUIRED

FAUST obtained 22 astronomical images during the ATLAS mission. Three of these were serendipitous observations while the shuttle realigned its guidance system, with integration times of about 5 minutes. The remaining observations had integrations of between 12 and 18 minutes. The observations were either pointed observations or scans across the sky up to 30° in length. In Table 1A we list the nominal pointing positions for the observations. The scanning observations are listed in Table 1B, and show the starting and ending positions for the scans. The second scan listed was observed twice.

We display the sky coverage of FAUST's observations in Galactic coordinates in Figure 3. The size of the circles indicates the size of the FAUST field.

[1] Also Department of Astronomy, University of California.
[2] Also Space Sciences Laboratory, University of California.

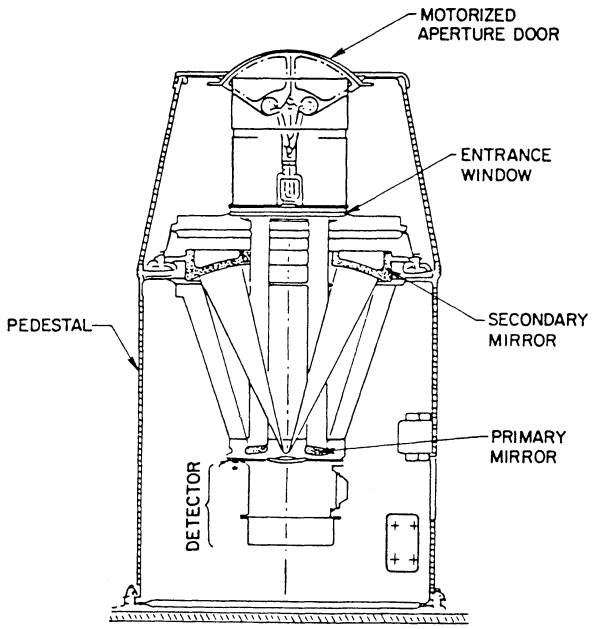

FIG. 1.—Functional diagram of the FAUST instrument, showing light paths.

4. DATA REDUCTION

For each photon detected, FAUST records the time and the position on the detector. This information was transmitted in real time and near real time through the space transportation system data network to our ground support equipment located at the NASA Marshall Space Center in Huntsville, Alabama. The data were captured at the transmission rate of 4 megabits s^{-1} and written to 8 mm format tape storage. Additionally, the images were displayed and inspected in real time.

We corrected for several instrumental and observational artifacts in the data to achieve a true picture of the sky. These corrections include removing the effects of shuttle drift during the exposure, correcting for airglow effects, removing optics and detector distortions, and correcting for detector quantum efficiency variations. The correction steps used in reducing the data are described in turn.

The FAUST instrument was fixed in the shuttle bay. Pointing the instrument was accomplished by moving the entire shuttle to the desired orientation. The dead band for FAUST operations was 1°. (The dead band specifies the angular deviation from the requested pointing when attitude correction thrusters were activated.) In order to form the image of an object that moved over the face of the detector, we derived our near-instantaneous pointing by accumulating for a few seconds photons from one or more bright stars in the field of view. The lengths of the short integrations were determined by the criterion that the drift during the integration should be a fraction

TABLE 1A

FAUST OBSERVATIONS: POINTINGS

Number	R.A.	Decl.	Remarks
1	0^h40^m	−72°.5	Small Magellanic Cloud
2	4 16	−56.3	Dorado galaxy cluster
3	5 10	−70.0	Large Magellanic Cloud
4	7 37	5.3	Alignment pointing
5	7 45	−19.2	PKS 0745
6	8 21	−59.4	Alignment pointing
7	12 0	−18.6	NGC 4038/39
8	12 2	17.9	Near North Galactic Pole
9	12 28	12.7	Virgo cluster
10	12 28	15.7	Virgo cluster
11	12 28	9.7	Virgo cluster
12	12 39	−1.2	Alignment pointing
13	12 40	22.0	Near North Galactic Pole
14	12 46	−41.0	Centaurus galaxy cluster
15	12 57	28.3	Coma galaxy cluster
16	13 34	−29.6	M83
17	17 20	−20.0	Ophiucus molecular cloud
18	19 0	−60.1	NGC 6752
19	20 12	−46.7	Telescopium galaxy cluster

TABLE 1B

FAUST OBSERVATIONS: SCANS

Number	R.A.	Decl.	R.A. (h m)	Decl.	Remarks
20	10^h0^m	−10°	11^h40^m	−20°	Low Galactic emission region in Hydra
21	14 0	−30	12 40	−20	Low Galactic emission region in Hydra

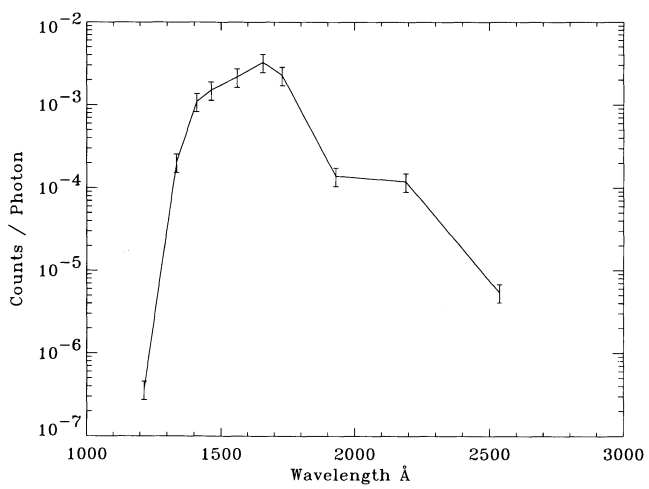

FIG. 2.—The wavelength response of the FAUST instrument, based on laboratory measurements and inflight calibration. Straight lines connect 10 calibration points in the wavelength range. The error bars indicate laboratory measurement errors only, not the systematic error discussed in text.

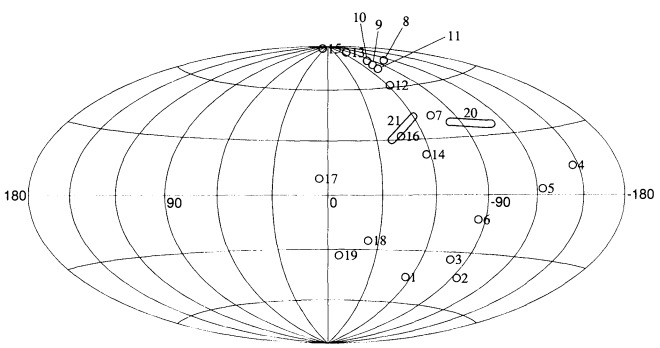

FIG. 3.—FAUST targets in Galactic coordinates. The size of the field of view is indicated by the circle. The number labels correspond with the numbers in Table 1.

of the overall instrument angular resolution, and were adjusted according to the orbiter drift rate. A correction for the rotation of the orbiter about an axis coaligned with the telescope axis was calculated from the shuttle's on-board pointing measurement system data. A master image was created by correcting the offset position and rotation of each of these short integrations and then co-adding them.

Because of orbiter motion and instrument vignetting, each point of the sky can receive a different effective exposure time. We correct for this effect in calculating fluxes by determining an exposure map from the series of sky positions actually observed. The photon flux is then calculated by dividing the map of the observed counts by the exposure map.

Because all FAUST photon data are time-resolved to better than 1 second, we can exclude unwanted data segments. Accordingly, we have excluded from our astronomical integrations data which show levels of contamination from airglow, twilight, attitude control thruster firings, aurora, and South Atlantic anomaly passages that would worsen the signal-to-noise ratio in the astronomical images. Shuttle and airglow emissions detected by FAUST are described in Lampton et al. (1993) and Chakrabarti et al. (1993). These emissions fall into three categories: (1) atmospheric recombination emission which diminishes gradually after crossing the terminator from day into night, (2) emission due to the interaction of orbiter's vernier attitude control thruster gas with the local atmosphere, and (3) emission from aurorae. Inspection of data containing the first two emissions show no small scale variation, but only a simple gradient across the field. Data including auroral emission occur in less than 20% of the images; these data are excluded from the astronomical images. The shuttle thruster firings appear as a featureless diffuse glow lasting a few seconds per incident (Lampton et al. 1993). This results in a local enhancement of the background. The total number of counts due to the source is usually quite small and always less than 5% of the total counts in an image. These regions are included in the current image reductions, because of the small size of this effect.

The detector is subject to three types of distortions which affect our spatial measurements. We attribute these to nonuniformities in the microchannelplate pores, radially dependent variations in the electrostatic fields, and a periodic effect due to the anode geometry and readout system. The first two effects lead to random distortions of photon positions, while the anode leads to a coherent, periodic remapping of photon positions along one of the anode axes. The net effect of all of these spatial distortions leads to a positional uncertainty of 2′, approximately the same size as the detector resolution.

We measured the effects of random distortions due to irregularities in the microchannel plates and accelerating fields within the detector during our ground-based calibration. We constructed an image by placing a mask of regularly spaced holes directly over the detector, and illuminating it. We then read out the difference between the actual and measured positions of photons striking the detector. We interpolated the distortion between these points by fitting a surface to the map of known points. We end up with a two-dimensional vector for each position on the detector, which describes the positional correction to be applied to each photon.

The pattern of wedges and strips on the anode gives rise to a periodic translation of photon positions along the strip direction making some pixels correspond to a larger region of sky than others. The frequency of this distortion is tied to the spatial frequency of strips in the detector anode, and corresponds to an angular scale of approximately 20′ on the sky. We correct for this distortion by remapping detected photons from their reported positions to a new grid of pixels of uniform size. The distance which a typical photon is moved is about 0.′5, or about one-sixth of the instrumental resolution, but the effect of this motion is to remove variations which appear at scales 40 times larger. This distortion map was added as a vector with the random corrections and applied to each photon in constructing an image.

We have considered three possible sources for flat field images to measure quantum efficiency variations across the detector. These are our laboratory calibration data, data taken in flight while the instrument was pointing down at the Earth's atmosphere, and data taken in flight while pointing towards the stars. After comparing these data sets, we have determined that the astronomical field data provide the most accurate flat field. We constructed the flat field from five separate images in the following manner. For each image, we searched for all sources at the 3 σ level. We then reaccumulated a separate picture from the data in detector coordinates, with photons from the instantaneous position of each star eliminated. The exposure map was adjusted accordingly. The resulting image was then normalized by the exposure map. The motion of the spacecraft ensured that each area of detector sampled many different view directions, both on and off sources. A final flat-field image was constructed by taking the average of five such sky exposures. Large-scale astronomical variations in the individual images had a standard deviation of less than 9%, leaving at most a residual large-scale mottling of 4% in the flat field image. The average number of counts per 2′ pixel in the flat field image was 7000, leading to a statistical knowledge of pixel-to-pixel variations in our flat field of better than 4%.

5. INSTRUMENT PERFORMANCE

5.1. *Field of View*

The usable field of view of FAUST is circular and 7.°6 in diameter. The edge of the field is set by the edge of the detector. We determined the exact angular scale on the detector by measuring the separation of stars of known position. Vignetting at the edges of the field is less than 10%. Because of spacecraft motion, the sky covered by FAUST during pointed observations is slightly larger than the instrumental field of view and is typically 10°. Additionally, for three of our observations, we chose to scan the instrument to cover a much larger region of sky, about 30° by 8°.

5.2. *Resolution*

The angular resolution achieved in the FAUST images is determined by the optics resolution, the detector resolution, and how well the image reduction process removes spacecraft motion. Our preflight calibration shows that the resolution of the detector alone is 2.′5 FWHM. The stars in images taken by FAUST during the mission have an average width (FWHM) of 3.′8. There is a slight worsening of the resolution near the edges of the frame (about 10%). Thus our image resolution is currently limited by spacecraft motion or possibly optical distortions. We may be able to improve the resolution as we refine our reduction process.

5.3. *Sensitivity*

We report here on a data set of point sources from 17 of the FAUST fields (excluding our scan and Magellanic Cloud data)

by applying an automatic source detection algorithm to them. For each pixel in these images, counts for a hypothetical star were summed from a circle of diameter 6′. A background measurement was made from an annulus outside of this region. A signal-to-noise figure for that pixel was formed, comparing the star counts to the background. A threshold was set such that we detected most of the sources apparent to visual inspection of the images. We detected more than 4800 sources by this method and obtained a flux measurement for each one. By analyzing the observed point spread function of stars, we determined that the flux measurement needed a correction factor of approximately 25% since not all of the stellar flux was contained in the inner circle. We applied this correction factor to the flux measurements.

We have carried out an in-flight calibration by comparing stellar fluxes measured by both FAUST and *IUE*. Approximately 450 *IUE* spectra from 78 objects observed by both FAUST and *IUE* were obtained from the National Space Science Data Center. We selected only large-aperture *IUE* data and reduced these spectra using the standard Regional Data Analysis Facility (RDAF) software. Each spectrum was background-subtracted so that the flux represents the astronomical signal which FAUST measures above any background local to FAUST. Each spectrum was inspected, and we excluded spectra in which a significant fraction of the flux was in emission lines, showed excessive contamination with reseaux obscurations, or showed continuum features not expected to be due to the astronomical source. We folded these spectra through the FAUST instrument response to obtain a flux measurement comparable to the FAUST photometry. Where there were multiple *IUE* measurements of a single object, we used the mean value. We list in Table 2 the *IUE* stars and spectra used for comparison, as well as the calculated *IUE* flux value in FAUST counts per second for each object.

To best reconcile the FAUST and *IUE* flux determinations, we first note that the uncertainties in the *IUE* fluxes we adopt (described below) are proportional to the flux, i.e., the logarithmic errors are equal among the comparison stars. Accordingly, we plot in Figure 4 the log of the fluxes measured by FAUST for each object versus the *IUE* value. The best linear fit to these points (in log form) is also plotted. In our best-fit calculation, we use 15.8% as the uncertainty of the *IUE* values, calculated as the squared sum of the average of the standard deviation of those *IUE* values with more than three measurements (13.4%) and the calibration uncertainties in the FAUST bandpass integral (8%). FAUST random errors (shown) are due to photon-counting statistics in the star and background, and are generally smaller than the other uncertainties. The small scatter of the 16 points about this line of unit slope confirms that there is a single conversion factor between FAUST and *IUE* measurements, with a best-fit value of 0.6 ± 0.09. Additionally, the small scatter shows that the FAUST instrument response is linear over the full range of comparison. We verified that our fit was not influenced by objects whose flux might be variable in the far-ultraviolet by refitting the data not including the quasar, QSO, galaxy, and two stars with the most significantly discrepant *IUE* measurements. We also refit the data using the standard deviation of the *IUE* measurements of the object as the *IUE* uncertainty, or 15.8% if there was only one measurement. In each case, the conversion factor changed by less than 10%, showing that this factor is not sensitive to the exact data or procedure used. We infer from this in-flight calibration that FAUST sensitivity had changed by about 40% since its preflight calibration. A lower sensitivity in-flight was also seen by other instruments on-board the ATLAS mission, possibly caused by contamination from material outgassing from the orbiter. We consider the comparison with *IUE* the best measure of the in-flight performance, since our last ground calibration occurred 2 years before the flight, and because of the possibility of in-flight contamination. This calibration shows FAUST to have a grasp of 2.6 ± 0.4 cm^2 sr Å. For a point source with a flat spectrum (an equal number of photons

TABLE 2

IUE COMPARISON STARS

Object Name	*IUE* Catalog Number	Equivalent *IUE* Flux Value (counts s^{-1})
Feige 66	SWP 03431	122.1
	SWP 24551	265.6
Feige 67	SWP 03358	58.4
HZ 43	SWP 07221	44.3
	SWP 14500	46.2
	SWP 14501	46.4
HD 62001	SWP 08866	44.3
	SWP 09153	84.0
GD 153	SWP 07448	27.3
HD 60825	SWP 32500	47.4
HD 112313; Longmore-Tritton 5	SWP 16896	13.6
	SWP 16897	12.5
	SWP 17236	13.2
	SWP 19909	12.8
HD 59771	SWP 26817	2.6
	SWP 27060	2.6
KUV 494−04 (Kiso UV object)	SWP 29996	7.1
PG 1302+283	SWP 32696	3.0
WD 0416−55	SWP 33106	3.3
NGC 4670	SWP 13533	1.5
ESO 141−G55	SWP 05514	2.6
	SWP 09200	2.1
	SWP 10269	3.0
	SWP 10298	3.4
	SWP 10301	3.7
	SWP 10643	2.6
	SWP 10644	2.5
	SWP 13453	2.3
	SWP 13454	2.4
	SWP 13617	2.5
	SWP 16428	2.0
	SWP 16560	2.1
	SWP 16788	2.2
	SWP 18091	1.9
	SWP 18095	1.7
	SWP 18241	1.7
	SWP 18383	1.4
	SWP 31563	1.8
3C 273	SWP 16790	5.9
	SWP 16801	6.1
	SWP 16802	6.4
	SWP 16803	6.2
	SWP 17300	7.1
	SWP 17301	7.5
	SWP 17302	7.3
	SWP 17303	7.0
	SWP 19731	4.5
	SWP 26489	5.0
	SWP 30238	5.0
	SWP 30239	5.0
	SWP 33907	5.2
	SWP 33908	5.2
WD 0418−53	SWP 10818	1.0
QSO 1229+204	SWP 16880	0.7
	SWP 16884	0.7
	SWP 20142	0.7

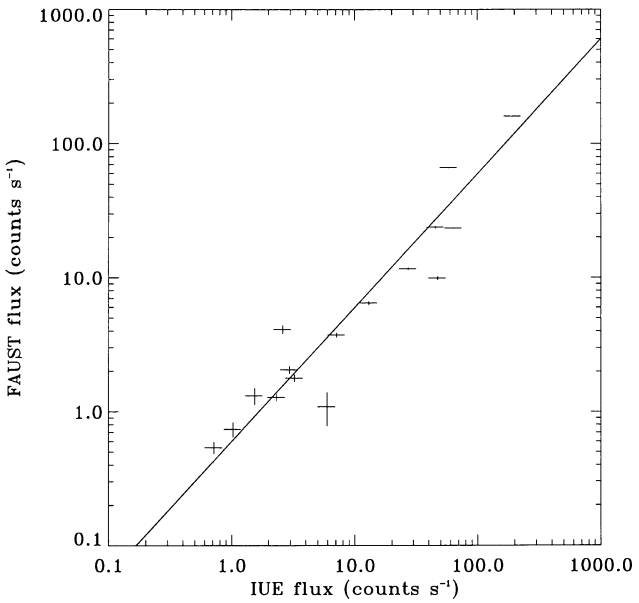

FIG. 4.—*IUE* and FAUST measurements of the same stars. The *IUE* low-dispersion spectra have been folded through the FAUST instrumental response for this comparison. The best χ^2 fit line is shown.

per Å), one multiplies FAUST counts per second by 5.3×10^{-3} to find the corresponding number of photons s^{-1} cm^{-2} Å^{-1}.

We next establish our detection limit. From the complete set of sources detected by FAUST described in § 5.3, we have created a histogram of the number of sources found as a function of their flux level. We display in Figure 5 two histograms, corresponding to sources found with the threshold set at 3 σ above the sky, and 5 σ above the sky. These two curves begin to diverge at a flux level of 6×10^{-14} ergs s^{-1} cm^{-2} Å^{-1}. Visual inspection indicates that most of the sources discovered at 3 σ are real sources. We conclude that sources with a flux of 1×10^{-14} ergs s^{-1} cm^{-2} Å^{-1} typically appear as 3 σ sources at our current level of analysis, and we have nearly complete

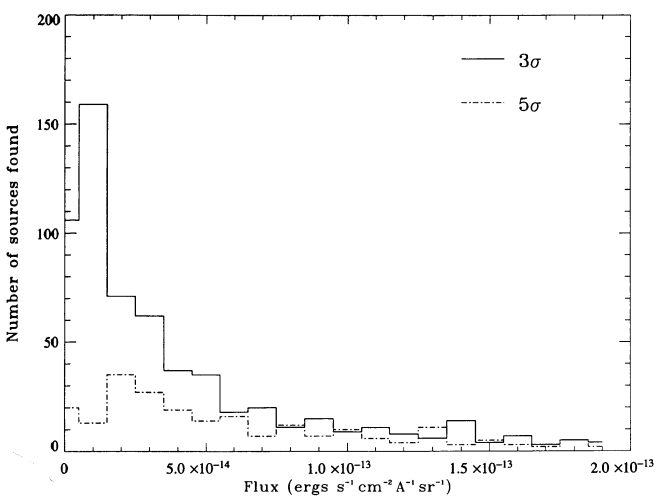

FIG. 5.—Histograms showing the number of sources found at 3 σ and 5 σ in our current images. Sources are detected to a threshold of 1×10^{-14} ergs s^{-1} cm^{-2} Å^{-1}.

detections of all sources above 6×10^{-14} ergs s^{-1} cm^{-2} Å^{-1}. Because each image had a different exposure time and varying observing conditions, the values given above are representative of the typical sensitivity in the FAUST images.

6. DISCUSSION

The *TD-1* satellite all-sky survey (Gondhalekar, Phillips, & Wilson 1980) provides the largest sample of sources detected at wavelengths similar to the FAUST bandpass. The *TD-1* survey data are available in several forms (Henry et al. 1988 and Thompson et al. 1978), but the most extensive list of sources is an electronic version (Landsman 1984), which has not yet been published. Nonetheless, this unpublished collection offers the most comprehensive catalog of point sources measured for a bandpass comparable to FAUST's. We utilize this electronic source to compare with FAUST measurements. The *TD-1* calibration is now known to the nonlinear at the faint end of the source list, where most of the overlap with FAUST sources occurs (Gondhalekar 1990). (Note that most of the flux in this band is due to stars from the bright end of the *TD-1* catalog, outside the range of comparison.) We therefore need to exclude from comparison *TD-1* sources fainter than 1.0×10^{-12} ergs s^{-1} cm^{-2} Å^{-1}. For stars at the brighter end of the overlapping source list, the FAUST detector can saturate when the number of photons incident on a single microchannel plate pore exceeds a few per second. We have examined FAUST stellar images for this effect and exclude from the comparison data from affected stars. These two limits include an overlap for fluxes between 1×10^{-12} and 2.5×10^{-11} ergs s^{-1} cm^{-2} Å^{-1}.

In Figure 6 we show a comparison of the flux measured for the same set of stars by FAUST and by *TD-1*. This figure includes stars, 8% of the total, added to the catalog based on their optical colors (Landsman 1984). The scatter in these data considerably exceeds that expected from quoted uncertainties of the *TD-1* measurements and the much smaller FAUST statistical uncertainties. Some effects which might introduce scatter into such a plot are the nonidentical bandpasses of FAUST and *TD-1*, stellar variability, and measurement errors by *TD-1* or FAUST. To investigate these possibilities, we have tested our photometry algorithm on simulated FAUST data and found only the expected statistical scatter in FAUST's photometric measurements. To evaluate the effect of the different bandpasses of the two instruments, we have subdivided the data shown in Figure 6 into sets including only stars of a single stellar type, A and B. The χ^2 for a linear fit to the data subsets was still more than 6 times larger than expected both for the given uncertainties and the fit to the *IUE* data. The wide variation of such a large fraction of the data independent of spectral type argues against stellar variability as the cause of the wide scatter. In view of the wide scatter in the *TD-1* data when compared with FAUST measurements, and the good fit and low scatter of the FAUST and *IUE* fluxes, we conclude that the errors in the *TD-1* source measurements are considerably larger than previously quoted.

The current FAUST detection limit is more than an order of magnitude fainter than the *TD-1* catalog flux limit of 5×10^{-13} ergs s^{-1} cm^{-2} Å^{-1}. It can be inferred from Figure 5 that sources which were detected by *TD-1* make up no more than 12% of detected FAUST sources. As a further check of the relative sensitivity of FAUST and *TD-1*, we examined the *TD-1* sources in the FAUST field of the Coma cluster of galaxies. We plot in Figure 7 these sources on a map of the sky. We show *TD-1* sources brighter than 5×10^{-13} ergs s^{-1} cm^{-2}

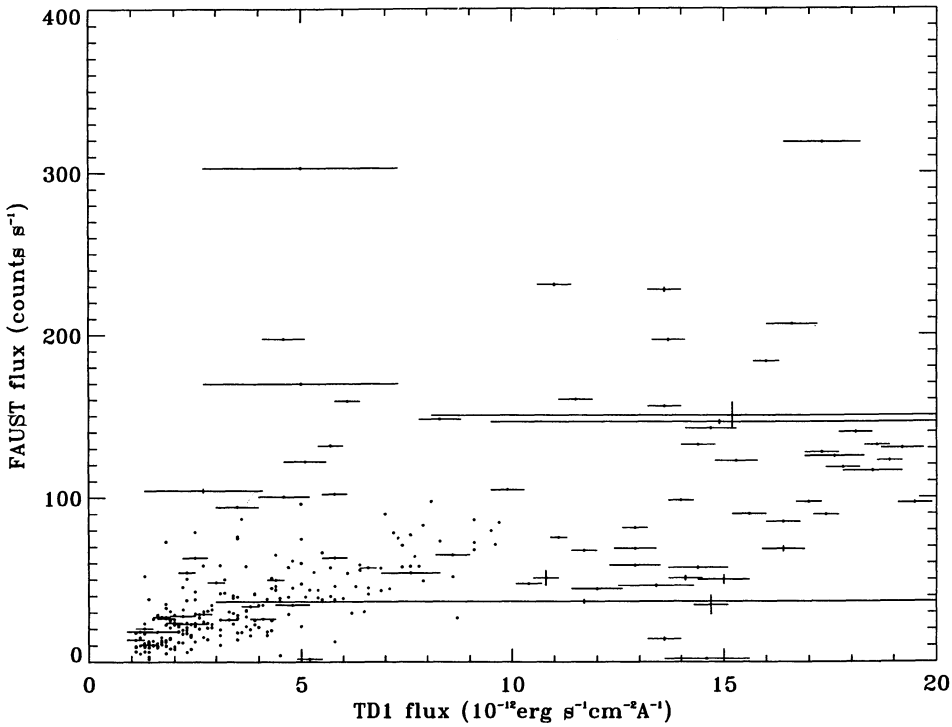

FIG. 6.—Set of stellar fluxes measured by both *TD-1* and FAUST. The uncertainties shown for FAUST are statistical, and the catalog values are shown for *TD-1*. Some error bars have been omitted for clarity.

Å^{-1}, and FAUST sources detected at 4 σ. There are four sources detected by *TD-1*, and 53 detected by FAUST. FAUST detects all the *TD-1* sources. No new sources above the *TD-1* limit were detected by FAUST.

The North Galactic Pole region was studied in detail by Brosch et al. (1993, in preparation). Many of the sources were identified with cataloged stars of galaxies and the rest were identified using spectroscopy from the Wise Observatory. Among 48 sources there are three white dwarfs, four galaxies, and 30 A–F stars. The projected density of sources agrees with the model of the Galaxy in the UV (Brosch 1991).

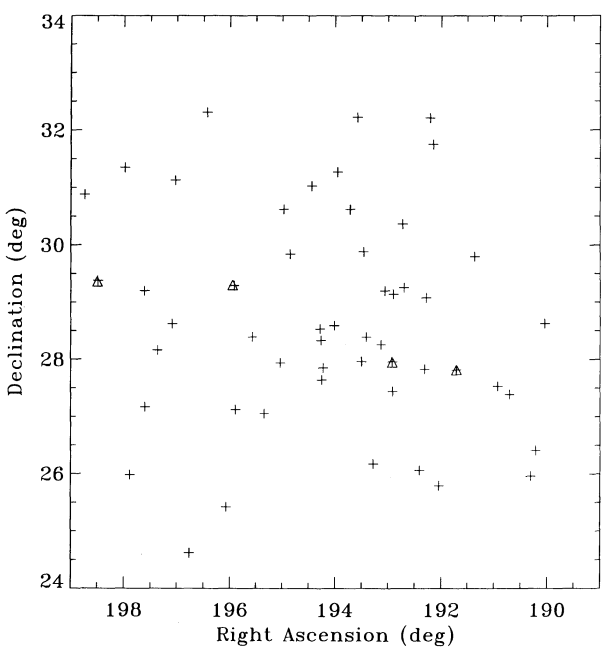

FIG. 7.—Sky map of the Coma cluster, showing FAUST sources detected (*crosses*), and *TD-1* sources detected (*triangles*). The *TD-1* sources shown are those above the published catalog's limiting sensitivity.

7. FUV EXCESS OBJECTS

We have begun to identify optical counterparts for each of the FAUST sources. In this work we have started with the Michigan Sky Survey (Houk & Cowley 1975) and the SAO Catalog (SAO Staff 1966). We have found optical counterparts in at least one of these catalogs for roughly the brightest 25% of FAUST sources. We show in Figure 8 the ratio of the FUV flux (measured by FAUST) to the cataloged visible flux plus a constant, versus the spectral type of the object. Most of the points group in a fairly well-defined locus, but a significant number of outlying objects show a substantial FUV excess. We have arbitrarily separated these with the line shown; about 5% of the points lie to the right of this line. This identifies about 90 objects as showing FUV excess. Some of these are in crowded fields where there is possible confusion with another bright UV source. We are currently seeking to identify these cases by several methods. We have examined each of the fields for other SAO or Michigan Sky Survey stars, and have eliminated from the list cases where another listed source could explain the FUV excess. For the remaining 60 sources, we are searching the SIMBAD and StarCat online data bases for sources at the locations of the FUV excess objects. Sources which appear interesting or which we are not able to identify will be observed spectroscopically to search for hot companion stars or other unusual objects. There results will be reported elsewhere.

8. CONCLUSIONS

FAUST's flight on broad the ATLAS-1 Spacelab mission has provided new astronomical data on FUV sources. We have

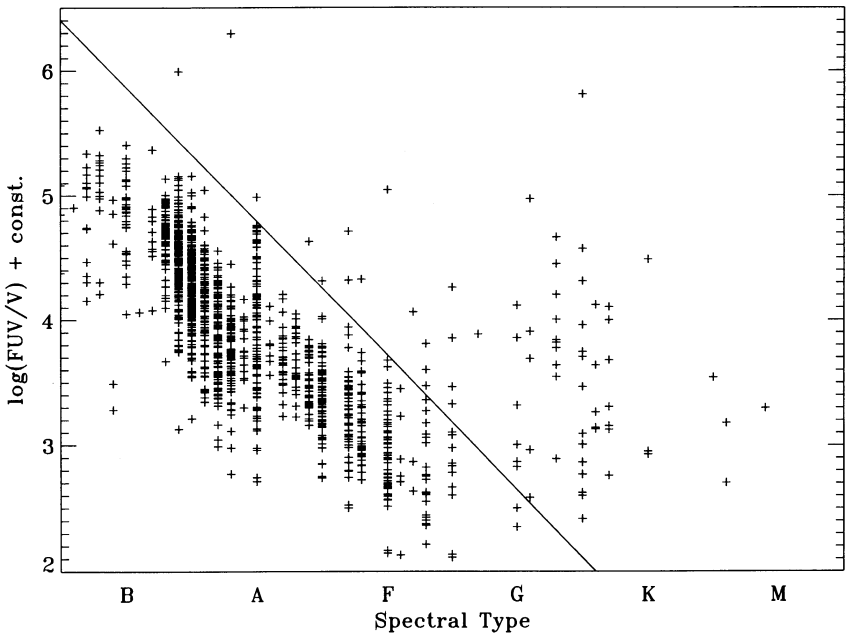

FIG. 8.—log of the FUV/visible flux ratio vs. spectral type for the brightest 25% of FAUST sources, for which we currently have spectral classifications. The arbitrary line shown separates those objects that show a substantial FUV excess.

obtained photometry of more than 4800 FUV sources with a detection threshold of 1×10^{-14} ergs s^{-1} cm^{-2} $Å^{-1}$, which is more than an order of magnitude more sensitive than the *TD-1* survey. We show that *TD-1* flux measurements have a much wider scatter than their claimed uncertainties. Finally, we have identified a number of FUV excess objects among the FAUST sources.

This research is supported by NASA contract NAS8-32577 and the CNES Science Program. We would like to thank Jean-Michel Deharveng and Noah Brosch for helpful suggestions, Patricia Pitts of the *IUE* project for assistance in identifying common FAUST and *IUE* sources, and Jayant Murthy for helpful criticisms. Stuart Bowyer acknowledges support from the John Simon Guggenheim Memorial Foundation.

REFERENCES

Bixler, J., Bowyer, S., Deharveng, J. M., Courtes, G., Malina, R. F., Martin, C., & Lampton, L. 1984, Science, 224, 184
Brosch, N. 1991, MNRAS, 250, 780
Chakrabarti, S., Sasseen, T. P., Lampton, M., & Bowyer, S. 1993, Geophys. Res. Lett., 20, 535
Craven, P. D., & Torr, M. R. 1988, NASA Tech. Memor. 4101
Deharveng, J. M., Riviere, G., Monnet, G., Moutonnet, J., Courtes, G., Deshayes, J., & Berges, J. 1979, Space Sci. Instr., 5, 21
Gondhalekar, P. M. 1990, in IAU Symp. 139, The Galactic and Extragalactic Background Radiation, ed. S. Bowyer & C. Leinert (Dordrecht: Reidel), 449
Gondhalekar, P. M., Phillips, A. P., & Wilson, R. 1980, A&A, 85, 272
Henry, R. C., Landsman, W. B., Murthy, J., Tennyson, P. D., Wofford, J. B., & Wilson, R. 1988, Atlas of the Ultraviolet Sky (Baltimore: Johns Hopkins Univ. Press)
Houk, N., & Cowley, A. P. 1975, University of Michigan Catalog of Two-Dimensional Spectral Types for the HD Stars, I–IV (Ann Arbor: Univ. Michigan)
Lampton, M., Deharveng, J. M., & Bowyer, S. 1990, in IAU Symp. 139, The Galactic and Extragalactic Background Radiation, ed. S. Bowyer & C. Leinert, 449
Lampton, M., Sasseen, T. P., Wu, X., & Bowyer, S. 1993, Geophys. Res. Lett., 20, 539
Lampton, M., Siegmund, O. H. W., Bixler, J., & Bowyer, S. 1986, in Proc. SPIE, 627, 383
Landsman, W. 1984, Ph.D. thesis, Johns Hopkins Univ.
Siegmund, O. H. W., Lampton, M., Bixler, J., Vallerga, J. V., & Bowyer, S. 1987, IEEE Trans. Nuc. Sci., NS-34, 41
Smithsonian Astrophysical Observatory Staff. 1966, Pub. Smithsonian Inst. Washington, DC, No. 4652 (Washington: Smithsonian Inst.)
Thompson, G. I., Nandy, K., Jamar, C., Monfils, A., Houziaux, L., Carnochan, D. J., & Wilson, R. 1978, Catalog of Stellar Ultraviolet Fluxes (Baghdad: Science Research Council)
Wynne, C. G. 1969, J. Opt. Soc. Am., 59, 572